Data-driven phase-isostable reduction for optimal nonfeedback stabilization of cardiac alternans

Tuhin Subhra Das and Dan Wilson

Phys. Rev. E **103**, 052203 — Published 3 May 2021

DOI: 10.1103/PhysRevE.103.052203

Data-Driven Phase-Isostable Reduction for Optimal Nonfeedback Stabilization of Cardiac Alternans

Tuhin Subhra Das[1] and Dan Wilson[1]

[1]Department of Electrical Engineering and Computer Science, University of Tennessee, Knoxville, TN 37996, USA

April 9, 2021

Abstract

Phase-isostable reduction is an emerging model reduction strategy that can be used to accurately replicate nonlinear behaviors in systems for which standard phase reduction techniques fail. In this work, we derive relationships between the cycle-to-cycle variance of the reduced isostable coordinates for systems subject to both additive white noise and periodic stimulation. Using this information, we propose a data-driven technique for inferring nonlinear terms of the phase-isostable coordinate reduction framework. We apply the proposed model inference strategy to the biologically motivated problem of eliminating cardiac alternans, an arrhythmia that is widely considered to be a precursor to more deadly cardiac arrhythmias. Using this strategy, by simply measuring a series of action potential durations in response to periodic stimulation, we are able to identify energy-optimal, nonfeedback control inputs to stabilize a period-1, alternans-free solution.

1 Introduction

Nonlinear oscillations are of key importance in the physical, chemical, and biological sciences. In high-dimensional settings, phase reduction is often used as a first step to analyze the oscillations in greater mathematical detail [8], [19] and to implement effective control strategies to produce desired behavior [22], [18], [30], [41]. While phase reduction is a well-established theoretical framework for analyzing the dynamical behaviors of weakly perturbed oscillatory systems, its underlying assumptions often break down as the magnitude of control input becomes large necessitating the incorporation of additional information.

Model reduction strategies based on the Koopman operator [5], [27], [28] have seen a surge of interest in the past decade as a framework by which the fundamental properties of a nonlinear dynamical system can be analyzed in a reduced order setting. The Koopman operator framework can be used to represent the dynamics of a fully nonlinear dynamical system in terms of a linear but infinite dimensional operator. In principle, a reduced order model of a nonlinear dynamical system can be obtained by finding a suitable finite-dimensional basis of Koopman eigenmodes [42]. General techniques such as dynamic mode decomposition (DMD) [39], [24], extended DMD [46], deep learning approaches [57], [25], and delay embeddings [1], [4] have all been proposed to identify suitable bases in various contexts.

In this work we consider the phase-isostable coordinate framework [51], [47] that characterizes the slowest decaying Koopman eigenmodes of an oscillatory dynamical system. While strategies

have been developed for computation of all of the necessary terms of the phase-isostable reduction when the right hand side of the underlying equations are known [47], [50], robust strategies have yet to be developed to compute the reduced functions in experimental situations where the full equations are not known but data is readily available. In light of these limitations, as a primary contribution of this work, an experimentally feasible strategy for computation of nonlinear terms of the phase-isostable reduced equations is proposed and illustrated. This strategy explicitly considers the change in variance of the isostable coordinates associated with entrained oscillations on a cycle-by-cycle basis in the presence of white noise. This information is then used to infer the nonlinear terms of the corresponding phase-isostable reduction.

The resulting reduced order model is used to implement and evaluate a nonfeedback control strategy for eliminating cardiac alternans in a computational model of an excitable cardiomyocyte [32]; the alternans arrhythmia is widely viewed as a precursor to cardiac fibrillation [31], [7] and subsequent cardiac arrest. From a dynamical systems perspective, alternans emerges as a result of a period doubling bifurcation [45], whereby the principle Floquet exponent of a periodic orbit transitions from a negative to a positive value. Previous authors have developed feedback control strategies for stabilizing the resulting unstable period-1 orbit, thereby eliminating alternans [12], [6], [55]. Here, we investigate a nonfeedback control strategy suggested in [48] for achieving the same objective; nonfeedback methods can be particularly useful for biological applications when real-time measurements of the system's state can be difficult to obtain. Using our proposed strategy, by simply measuring a series of action potential durations in response to periodic stimulation, we are able to identify energy-optimal, nonfeedback control inputs to stabilize a period-1, alternans-free solution.

The organization of this paper is as follows: Section 2 provides a background on cardiac alternans as well as a summary of the phase and isostable coordinate reduction framework used in this work. In Section 3, we leverage the isostable coordinate reduction framework to identify an energy-optimal, nonfeedback control strategy for eliminating alternans. We subsequently propose a data-driven strategy to infer the terms of the reduction necessary to implement this optimal control strategy. This strategy only requires measured information about the action potential durations of the cardiac action potentials (as could be measured in an experimental setting) and does not require any information about the underlying system equations. Section 4 illustrates and evaluates the resulting control strategy, and Section 5 provides concluding remarks.

2 Background

Here, we provide background information about the motivating problem of developing a nonfeedback control strategy for eliminating cardiac alternans as well as the phase-isostable-based reduced order modeling frameworks that will be used in this work.

2.1 Models for the Dynamical Behavior of Excitable Cardiomyocytes and the Emergence of Cardiac Alternans

Consider a general model for the cellular behavior of a single cardiomyocyte

$$\begin{aligned} C_{\mathrm{m}}\frac{dV}{dt} &= -(I_{\mathrm{ion}}(V,m) + I_{\mathrm{ext}}(t)) + \epsilon\eta(t) + \alpha u(t), \\ \frac{dm}{dt} &= f_m(V,m). \end{aligned} \tag{1}$$

Above, V denotes the transmembrane voltage, $m \in \mathbb{R}^N$ is a collection auxiliary variables that can be used to represent ion concentrations, gating variables, and other dynamical processes, I_{ext} represents the influence of an external pacemaker, I_{ion} is a collection of ionic currents, f_m sets the dynamics of the auxiliary variables, C_m is the membrane capacitance, $\eta(t)$ is a unit intensity, independent and identically distributed noise process, and both $0 < \epsilon \ll 1$ and $0 < \alpha \ll 1$. Additionally, $u(t)$ is a transmembrane current input (in $\mu\text{A/cm}^2$) used for control and will be considered later. Most cardiac cells are excitable, and the external pacemaker $I_{\text{ext}}(t)$ sets the pacing rate in (1).

In this work, we will consider the Noble model [32] with model equations given in Appendix A. Here, we will take $I_{\text{ext}}(t) = -150\exp(-(\text{mod}(t, T_{\text{pace}}) - 8)^2)$. This pacemaker input provides a periodic input to elicit action potentials at a pacing period T_{pace}. Representative behavior of this model is shown in Figure 1 taking ϵ (which sets the noise intensity) to be 0.14. Cardiac cellular dynamics are often represented in terms of the beat-to-beat action potential durations (APDs), defined as the amount of time the transmembrane voltage remains depolarized above a certain threshold on a given action potential. For slower pacing rates action potentials are nearly constant on a beat-to-beat basis shown in panel A of Figure 1. As the pacing rate increases, a period doubling bifurcation occurs yielding stable period-2 behavior as shown in panel B.

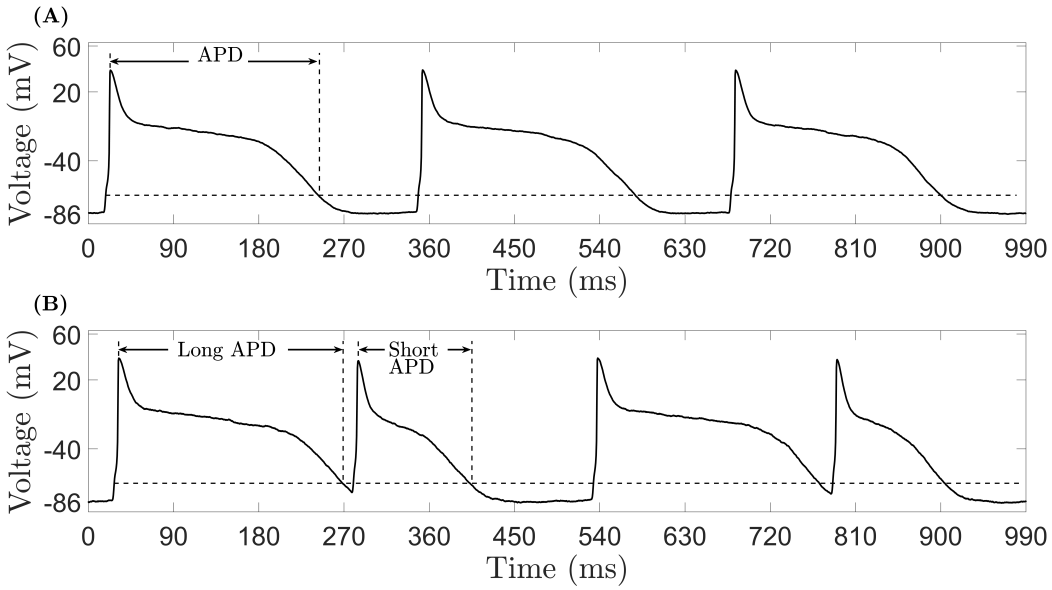

Figure 1: Steady state pacing of the Noble Model from Appendix A. Panel (A) illustrates representative period-1 behavior that occurs for slower pacing rates. Panel (B) shows representative period-2 behavior that emerges for faster pacing rates. This stable period-2 behavior is known as action potential duration alternans. On each beat, action potentials are taken to be the time between successive crossings of the -70 mV threshold, as denoted above with a dashed horizontal line.

The steady state period-2 behavior highlighted in panel B of Figure 1 is generally referred to as APD alternans, that is, a beat-to-beat alternation of the APD despite a constant rate of pacing. Cellular cardiac alternans is generally considered to be proarrhythmic as it can lead to dispersion of refractoriness in tissue, wavebreak, and subsequent transition to more lethal cardiac arrhythmias [45], [7], [13]. From a biological perspective, alternans is usually attributed to steep APD restitution [33], instabilities in the calcium cycling dynamics [34], or a combination of both factors [14]. From

a dynamical systems perspective, both calcium-driven and voltage-driven alternans arise due to a period doubling bifurcation. This work uses methods that are independent of the exact cause of the bifurcation (e.g., calcium or voltage driven alternans) and focuses on the problem from the point of view of eliminating the dynamical instability.

2.2 Isostable Coordinates and Phase-Amplitude Reduction

Towards applying a reduced order modeling framework for general cardiac cell models, the model equations (1) can be represented by a dynamical system that is entrained to an exogenous periodic input:

$$\begin{aligned} \dot{x} &= F(x) + I_{\text{ext}}(a) + \alpha I_{\text{inp}} + \epsilon I_{\text{noise}}(t), \\ \dot{a} &= 1. \end{aligned} \tag{2}$$

Here, $x \in \mathbb{R}^N$ is the state of the system ordered so that the first element corresponds to the transmembrane voltage variable and the remaining elements correspond the auxiliary variables, $I_{\text{ext}}(a)$ is a T_{pace}-periodic input with $a \in \mathbb{S}^1$ being a time-like variable that takes values in the range $[0, T)$ where T is a multiple of T_{pace}, $I_{\text{inp}} = \begin{bmatrix} u(t) & 0 & \dots & 0 \end{bmatrix}^T$, and $I_{\text{noise}} = \begin{bmatrix} \eta(t) & 0 & \dots & 0 \end{bmatrix}^T$. Letting $y \equiv \begin{bmatrix} x & a \end{bmatrix}^T \in \mathbb{R}^{N+1}$, define $y^\gamma(t)$ of (2) to be a periodic orbit (either stable or unstable) that exists in the absence of control and noise. In order to further analyze (2) in a reduced order setting we will consider the phase-isostable coordinate framework [51], [47]. This reduction strategy leverages Floquet theory [20] to define a set of exponentially decaying isostable coordinates (which can also be thought of as level sets of the Koopman eigenfunctions [28], [26] with decay rates governed by the Floquet exponents). It will be assumed that all but one of the nonunity Floquet multipliers of this orbit are close enough to zero so that only one isostable coordinate is required to characterize the dynamics transverse to the limit cycle. While somewhat restrictive, the single amplitude coordinate assumption has been successfully applied in a variety of other applications [29], [54], [49]. Here, we are considering dynamics that are close to a period doubling bifurcation in which a Floquet exponent transitions between positive and negative values. If none of the other Floquet exponents are close to zero, it is reasonable to expect that the salient dynamics can captured by this single, near-zero isostable coordinate. With these assumptions, one can use the isostable reduction framework to transform a general model of the form (2) to a phase-isostable based model of the form

$$\dot{\theta} = \omega + [Z(\theta) + \psi B(\theta)]\,(\alpha u(t) + \epsilon \eta(t)), \tag{3}$$

$$\dot{\psi} = \kappa \psi + [I(\theta) + \psi C(\theta)]\,(\alpha u(t) + \epsilon \eta(t)). \tag{4}$$

Here, θ is the phase coordinate which gives the timing of the oscillation, ψ is the isostable coordinate which characterizes deviations transverse to the limit cycle, $\omega = 2\pi/T$ is the natural frequency, κ is the principle Floquet exponent, $Z(\theta)$ and $I(\theta)$ are the phase and isostable response curves that characterize the response to inputs near the limit cycle, and $B(\theta)$ and $C(\theta)$ provide nonlinear corrections that are valid to first order accuracy in the isostable coordinate. Above, it is assumed that the noise intensity is small enough so that the Ito correction [11] can be ignored.

We note that while the periodic orbit of (1) results from an externally applied periodic input, when the system is augmented with a time-like variable in (2), it becomes autonomous and the notion of asymptotic phase is still applicable. For the moment, suppose that $y^\gamma(t)$ is stable (the case where $y^\gamma(t)$ is unstable is considered momentarily). At all locations in the basin of attraction of the entrained periodic orbit, the asymptotic phase can be represented using the notion of isochrons

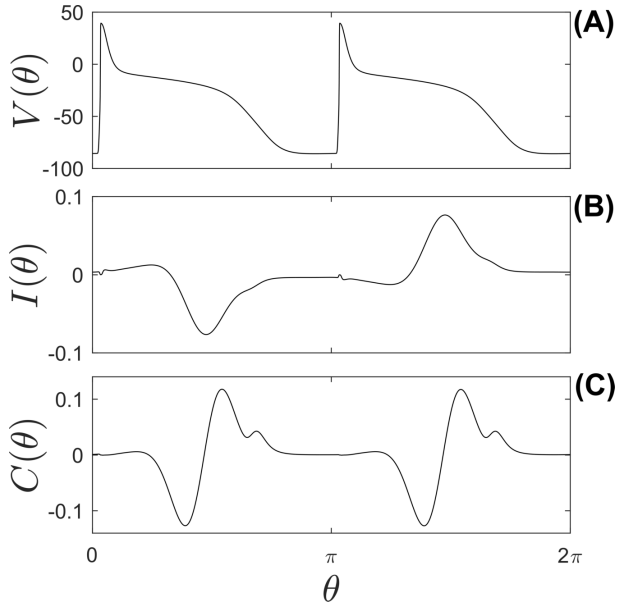

Figure 2: The panels above show relevent terms from the reduction (6). The Noble model from Appendix A is considered with a pacing rate of 290 ms. As described in the text, two action potentials are used to define the periodic orbit so that the resulting Floquet multipliers are positive. Panel (A) shows the voltage trace on the periodic orbit, with panels (B) and (C) giving the corresponding values of $I(\theta)$ and $C(\theta)$, respectively.

[15], [56] which are defined as follows: in the absence of noise and control, for any initial condition $y(0) \in y^\gamma(t)$ the isochron associated with $y(0)$ is given by the set of all $w(0)$ for which $\lim_{t\to\infty} ||y(t) - w(t)|| = 0$. Recall that in (2) it is assumed that the periodic orbit is entrained to the periodic input $I_{\text{ext}}(a)$ so that the time-like variable, a, alone determines the asymptotic phase; using the aforementioned definition of isochrons, one can show that $\theta = \text{mod}(\theta_0 + 2\pi a/T, 2\pi)$ (cf. [47]) where θ_0 is a constant that can be defined arbitrarily. For simplicity of exposition, we will define the phase so that $\theta_0 = 0$. We take $a = 0$ when $t = 0$ so that

$$\theta = \text{mod}(2\pi t/T, 2\pi). \tag{5}$$

Consequently, the phase dynamics in (3) can be eliminated yielding a single equation to describe the evolution of the isostable coordinates

$$\dot{\psi} = \kappa\psi + [I(\omega t) + \psi C(\omega t)]\,(\alpha u(t) + \epsilon\eta(t)). \tag{6}$$

In general, phase reduction alone (i.e, using only (3)) is not sufficient to study the behavior of entrained systems such as (1). Indeed, the direct relationship (5) makes the study of the phase dynamics trivial. However, the incorporation of isostable coordinates allows for the stability of entrained solutions to be analyzed with Equation (6). Figure 2 shows the terms of Equation (6) for the Noble model from Appendix A with a pacing period of $T_{\text{pace}} = 290$ ms. The Floquet multiplier associated with a single action potential at this pacing rate over a single cycle is -0.85 which would yield an imaginary Floquet exponent making subsequent analysis difficult. In order to yield a positive Floquet multiplier, two action potentials are used to define the periodic orbit with an overall period of $T = 2T_{\text{pace}}$ yielding a Floquet multiplier of 0.723 and an associated Floquet

exponent $\kappa = \log(0.723)/T = 5.6 \times 10^{-4}$. Panel (A) of Figure 2 shows the transmembrane voltage with the associated values of $I(\theta)$ and $C(\theta)$ in panels (B) and (C), respectively. These terms are computed numerically using strategies suggested in [47]. As shown in Appendix B, $I(\theta) = -I(\theta+\pi)$.

Finally, the simplification (5) that ultimately yields (6) is obtained assuming that the entrained periodic orbit is stable so that the notion of isochrons can be used. In Appendix C, we illustrate that even for an unstable orbit, Equations (5) and (6) can still be used to characterize the phase and isostable dynamics when both noise and applied transmembrane current are small.

3 A Data-Driven Model Identification Strategy and Optimal Design of Periodic Inputs to Eliminate Alternans

The analysis in this section is motivated by the design of inputs $u(t)$ that can be used to modify the stability of an entrained solution of (2). In the absence of input and noise, the associated equation for the reduced isostable dynamics from (6) has a fixed point at $\psi = 0$. The stability of this solution is governed by the sign of $\mathrm{Re}(\kappa)$, with $\mathrm{Re}(\kappa) < 0$ (resp., $\mathrm{Re}(\kappa) > 0$) corresponding to stable (resp., unstable solutions). When the period doubling bifurcation that results in alternans occurs, the period-1, alternans-free solution loses stability (i.e., its associated Floquet exponent crosses zero) and a stable period-2 solution associated with alternans emerges. From a dynamical perspective the problem of eliminating alternans can be framed as a problem of finding a periodic input that yields a periodic orbit with with $\kappa < 0$. In [48] it was shown that when applying a T-periodic input $\alpha u(t)$ to (6) the Floquet exponent of the shifted periodic orbit is modified according to

$$\Delta\kappa = \frac{\alpha}{T}\int_0^T C(\omega t)u(t)dt. \tag{7}$$

Equation (7) provides a guide from which to design nonfeedback stimuli to modify the stability of a periodic orbit. This strategy, however, requires explicit knowledge of $C(\theta)$. In situations where the dynamical equations from (2) are known, it is relatively straightforward to compute the terms in the reduction (3) and (4) numerically using methods described in [47]. However, in many experimental applications, the dynamical equations are usually not known accurately enough to be used for control purposes. Previous authors have developed strategies for measuring phase response curves for experimental systems using a 'direct method' [19], [10] and related strategies have been proposed for computing $I(\theta)$ and $B(\theta)$ [53]. However, no experimentally feasible strategies currently exist that can be used to infer the term $C(\theta)$ which is necessary for implementation of Equation (7). The analysis to follow provides a strategy whereby the shape of $C(\theta)$ from (6) can be inferred by understanding how statistical properties of the isostable coordinates change in response to periodic forcing in a noisy environment.

3.1 Optimal Elimination of Alternans Using Periodic Stimulation to Stabilize the Underlying Period-1 Orbit

In previous work [48], a strategy was developed for identifying an energy-optimal strategy to stabilize an unstable periodic orbit using a periodic control input. A modified strategy based on this approach is presented here for stabilizing an unstable period-1 alternans-free solution of (2). The optimal control derivations presented below take $\eta(t) = 0$ in (6), assuming that noise intensity in the full system is too small to significantly influence the Floquet exponents of the periodic solution. To begin, suppose that the unstable periodic orbit has only one unstable Floquet multiplier, with the remaining nonunity Floquet multipliers being small enough in magnitude so that their

associated dynamics can be effectively ignored. Such a system can be represented according to the isostable coordinate reduction (6),

$$\dot{\psi} = \kappa\psi + [I(\omega t) + \psi C(\omega t)]\, u(t), \tag{8}$$

where κ is the unstable Floquet exponent, $I(\theta)$ is the isostable response curve, $C(\theta)$ is a first order correction for the isostable dynamics, and $\omega = 2\pi/T$ where T is the period. In the above isostable reduced equation, α has been absorbed into $u(t)$ for simplicity of exposition. As discussed in Section 2.2, because the dynamics are entrained to an external pacemaker, the phase $\theta = \omega t$ and cannot be influenced by $u(t)$.

Recall that we take the total period of oscillation to be $T = 2T_{\text{pace}}$. Letting $u(t)$ be a T-periodic input, notice that (8) is T-periodic. Additionally, because $u(t)$ and ψ are both assumed to be small, (8) is of the general form $\dot{x} = \epsilon F(x,t)$ and formal averaging [38], [16] can be applied to represent (8) as

$$\dot{\Psi} = (\kappa + \zeta)\Psi + \nu, \tag{9}$$

where $\zeta = \frac{1}{T}\int_0^T C(\omega s)u(s)ds$, $\nu = \frac{1}{T}\int_0^T I(\omega s)u(s)ds$, and Ψ provides a close approximation for ψ when using the averaging framework. Fixed points of Equation (9) correspond to periodic orbits of the unaveraged equations (8) with the same stability so that ζ gives the effective change in the Floquet multiplier resulting from the application of $u(t)$.

Towards the formulation and solution of an optimal control problem to stabilize an unstable solution of (8) (and consequently stabilize the period-1 alternans-free solution of (2)), we seek to find a stimulus that minimizes $\int_0^T u^2(t)dt$ subject to the constraint $\kappa + \zeta = \kappa^{\text{targ}}$, where κ^{targ} is a target Floquet exponent for the stabilized solution. As noted in [48], this constraint is satisfied provided the differential equation

$$\dot{R} = C(\omega t)u(t) + \kappa, \tag{10}$$

with boundary conditions $R(0) = 0$ and $R(T) = T\kappa^{\text{targ}}$ is satisfied. Consequently, the goal of finding an energy-optimal, periodic stimulus to stabilize the unstable periodic can be posed as a calculus of variations problem [21] which seeks to minimize the cost functional

$$\mathcal{M}[R, \dot{R}, u(t)] = \int_0^T \left(u^2(t) + L_1(\dot{R} - C(\omega t)u(t) - \kappa)\right)dt, \tag{11}$$

where L_1 is a Lagrange multiplier that forces the dynamics to satisfy (10). Associated Euler-Lagrange equations are

$$\frac{\partial M}{\partial u} = \frac{d}{dt}\left(\frac{\partial M}{\partial \dot{u}}\right), \tag{12}$$

$$\frac{\partial M}{\partial R} = \frac{d}{dt}\left(\frac{\partial M}{\partial \dot{R}}\right), \tag{13}$$

where M is the integrand of the cost functional (11). All extremal solutions of (11) must satisfy the Euler-Lagrange equations (12) and (13). The optimization problem can be further simplified, as done in [48], by noting that direct evaluation of (13) shows that $\dot{L}_1 = 0$ along extremal solutions so that L_1 is a constant. Evaluation of (12) shows that

$$u(t) = \frac{L_1 C(\omega t)}{2}. \tag{14}$$

Additionally, upon substituting (14) into (10) and manipulating, one finds that when the Lagrange multiplier

$$L_1 = \frac{2(\kappa_{\text{targ}} - \kappa)}{\frac{1}{T}\int_0^T C^2(\omega t)dt} \tag{15}$$

is chosen, the required boundary conditions of (10) are satisfied. Noticing that $\kappa_{\text{targ}} - \kappa < 0$ in (15), one finds $L_1 < 0$ so that the energy-optimal stimulus from (14) is proportional to $C(\omega t)$ and scaled by a negative constant.

As a final note, Equation (14) states that the optimal control inputs to stabilize the unstable alternans-free solutions of (1) are simply proportional to $C(\theta)$. The data-driven estimation strategy for $C(\theta)$ detailed in Section 3.5 is able to estimate $C(\theta)\mu$ where $\mu > 0$ is an unknown constant. The inability to compute the magnitude of $C(\theta)$ means that it is not possible to determine the magnitude of the optimal stabilizing input *a priori*. From a practical perspective, however, stabilization can still be achieved by applying an input $\xi C(\theta)$ where ξ is a negative constant and increasing the magnitude of ξ until stabilization is achieved. The resulting input will be energy-optimal in the sense that it shifts the Floquet exponent towards more negative values as efficiently as possible, i.e., the effective Floquet exponent $\kappa + \zeta$ when the periodic input is applied will be achieved using the minimum possible energy.

3.2 Exploiting Noise to Estimate $C(\theta)$ From the Phase-Isostable Reduced Equations

The section to follow details a strategy by which the shape of $C(\theta)$ from the reduced order equation (6) can be inferred by considering the variance of the isostable coordinates in response to noise. For the moment, we will take $u(t) = 0$ and it will be assumed that ψ remains an $\mathcal{O}(\epsilon)$ term in response to the $\mathcal{O}(\epsilon)$ noise. For the moment, we will assume that $\kappa < 0$ (We will consider situations where $\kappa > 0$ in Section 3.4). Under these assumptions, to leading order, (6) becomes

$$\dot{\psi} = \kappa\psi + \epsilon I(\omega t)\eta(t) + \mathcal{O}(\epsilon^2). \tag{16}$$

Introducing $r(t) \equiv \psi(t)e^{-\kappa t}$ one can write

$$\dot{\psi} = \dot{r}e^{\kappa t} + \kappa r e^{\kappa t} = \kappa r e^{\kappa t} + \epsilon I(\omega t)\eta(t). \tag{17}$$

Rearranging and simplifying yields

$$\dot{r} = \epsilon e^{-\kappa t} I(\omega t)\eta(t). \tag{18}$$

Directly integrating (18) yields

$$r(t) = r(t_0) + \epsilon \int_{t_0}^{t} e^{-\kappa s} I(\omega s)\eta(s)ds, \tag{19}$$

and finally,

$$\psi(t) = \psi(t_0)e^{\kappa(t-t_0)} + \epsilon \int_{t_0}^{t} e^{\kappa(t-s)} I(\omega s)\eta(s)ds. \tag{20}$$

We will consider (20) in a situation where t is sufficiently larger than t_0 so that $\psi(t_0)$ can be assumed to be zero. Letting $E[X]$ denote the expected value of the random variable X, $E[\psi(t)] = 0$ because the noise has zero mean. The variance is then

$$\begin{aligned} \text{var}(\psi(t)) &= E[(\psi(t) - E[\psi(t)])^2], \\ &= \epsilon^2 \int_{t_0}^{t} e^{2\kappa(t-s)} I^2(\omega s)ds, \end{aligned} \tag{21}$$

where the second line follows from the property that $(\int_{t_1}^{t_2} f(x)dx)^2 = \int_{t_1}^{t_2}\int_{t_1}^{t_2} f(x)f(y)dxdy$ along with the property of white noise that $E[\eta(s)\eta(s')] = \delta(s-s')$.

Next, consider the reduced order system under the application of a small sinusoidal input $u(t) = \alpha \sin(2\pi nt/T)$, where $n \in \mathbb{N}$ and $0 < \epsilon \ll |\alpha| \ll 1$. In other words, α is assumed to be small, but still significantly greater than the noise intensity. Suppose that the resulting input yields a periodic orbit of (2) that is still entrained to the external periodic input $I_{\text{ext}}(a)$. The resulting orbit $y^{\gamma*}(t)$ will be a version of $y^{\gamma}(t)$ that has been shifted by a small amount due to the incorporation of $u(t)$. This yields isostable dynamics similar to (6):

$$\dot{\psi^*} = (\kappa + \Delta\kappa)\psi^* + \epsilon\left[I(\omega t) + \Delta I(\omega t) + \psi^*(C(\omega t) + \Delta C(\omega t))\right]\eta(t). \tag{22}$$

Here ψ^* corresponds to isostable coordinate for the orbit $y^{\gamma*}(t)$. In (22), the periodic orbit is shifted slightly by the new application of $u(t)$ and the terms $\Delta\kappa$, $\Delta I(\omega t)$, and $\Delta C(\omega t)$ are included to account for resulting shifts in the reduced order equations. Note here that $y^{\gamma*}(t)$ is defined to be the entrained solution that results when $u(t)$ is applied; consequently $u(t)$ does not appear explicitly in (22). Once again, because the noise intensity is $\mathcal{O}(\epsilon)$, the magnitude of ψ^* is assumed to be an $\mathcal{O}(\epsilon)$ term.

Rewriting (22) to focus solely on the order ϵ terms from (22) yields

$$\dot{\psi^*} = (\kappa + \Delta\kappa)\psi^* + \epsilon(I(\omega t) + \Delta I(\omega t))\eta(t) + \mathcal{O}(\epsilon^2) \tag{23}$$

Noting the similarity between (16) and (23), we find that $E[\psi^*] = 0$ and

$$\text{var}(\psi^*(t)) = E[(\psi^*(t) - E[\psi^*(t)])^2] = \epsilon^2 \int_{t_0}^{t} e^{2(\kappa+\Delta\kappa)(t-s)}(I(\omega s) + \Delta I(\omega s))^2 ds. \tag{24}$$

Recalling that $u(t)$ is an $\mathcal{O}(\alpha)$ term, $\Delta\kappa$ and $\Delta I(\omega s)$ are also $\mathcal{O}(\alpha)$ terms. With this in mind, expansion of (24) and subsequent comparison to $\text{var}(\psi)$ yields

$$\begin{aligned}\text{var}(\psi^*) - \text{var}(\psi) &= \Delta k\, \underbrace{\epsilon^2 \int_{t_0}^{t} \left[2e^{2\kappa(t-s)} I^2(\omega s)(t-s)\right] ds}_{\beta} \\ &\quad + \underbrace{2\epsilon^2 \int_{t_0}^{t} \left[e^{2\kappa(t-s)} I(\omega s) I'(\omega s) \Delta I(\omega s)\right] ds}_{\rho} + \mathcal{O}(\alpha^2) \\ &= \Delta\kappa\beta + \rho, \end{aligned} \tag{25}$$

where $' \equiv d/d\theta$. Equation (25) can be simplified further by noting, as shown in Appendix B, that for the models considered in this work, i.e., those that yield negative Floquet multipliers when the overall period is comprised of a single action potential, $I(\theta) = -I(\theta + \pi)$. Hence, $\Delta I(\theta) = -\Delta I(\theta + \pi)$ and $I'(\theta) = -I'(\theta + \pi)$ as well. With this in mind, considering the structure of ρ and β, in situations where κ is small so that the decay of $e^{2\kappa(t-s)}$ is slow, the integrand governing ρ will take positive and negative values that tend to balance out and ρ will be small relative to β. This is indeed the case for our numerical model – using the reduced order model associated with the $T_{\text{pace}} = 290$ ms pacing rate, $\Delta\kappa\beta$ is more than 1000 times larger in magnitude than ρ. Therefore, we assume that ρ is negligible in (25) allowing (7) can be substituted into (25)

to yield

$$\begin{aligned}\mathrm{var}(\psi^*) - \mathrm{var}(\psi) &= \frac{\beta}{T}\int_0^T C(\omega t)u(t)dt \\ &= \frac{\alpha\beta}{T}\int_0^T C(\omega t)\sin(2\pi nt/T)dt \\ &= \frac{\alpha\beta}{2}b_n, \end{aligned} \tag{26}$$

where b_n is the n^{th} term of the Fourier series expansion of $C(\omega t)$. An identical argument (using cosine wave inputs instead of sine waves) can be followed to provide relations for the other terms of the Fourier series expansion

$$C(\omega t) = a_0/2 + \sum_n \left(b_n \sin(2\pi nt/T) + a_n \cos(2\pi nt/T)\right). \tag{27}$$

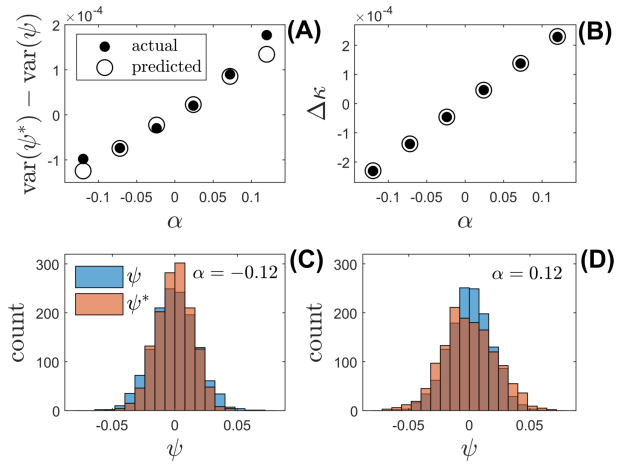

Figure 3: Numerical confirmation of the derived relationships between changing Floquet multipliers and the variance of the resulting isostable coordinates for simulations of (16) and (23). Black dots in panel (A) show how the variance of the isostable coordinates changes when input $u(t) = \alpha\sin(8\pi t/T)$ is applied. Predictions computed according to (25) are shown as open circles. Histograms of the measurements of the isostable coordinates obtained from simulations of (16) and (23) are shown in Panels (C) and (D) providing a visual representation of the change in variance that results when sinusoidal input is applied. Note that overlapping regions of the histograms in panels (C) and (D) appear brown.

Panel (A) of Figure 3 provides a numerical confirmation of the relations (25) using the Noble model with a pacing rate of 290 ms. Noise with intensity 2×10^{-4} is used to simulate the associated reduced order model (16) and the value of ψ is stored after every $10T$ units of time. Next, in the absence of noise, $u(t) = \alpha\sin(8\pi t/T)$ (i.e., a sinusoid with a period that corresponds to half the pacing period) is applied and the resulting reduced order terms are computed. Once these terms are identified, simulations of (23) are performed using noise with the same intensity and the variance of the measurements of the isostable coordinates are compared. Black dots in panel (A) of Figure 3 shows the difference in variance between simulations as a function of α with open circles computed according to (25). Panels (C) and (D) show distributions of ψ and ψ^*, taken from simulations of

(16) and (23), respectively. In panel (B), the actual change in the Floquet exponent is compared to the value predicted by the relationship (7).

3.3 Relating the Variance of the Isostable Coordinates to Measurable Data

Equation (26) illustrates how sinusoidal inputs influence the variance of the isostable coordinates in relation to the terms of the Fourier expansion of $C(\omega t)$. However, the isostable coordinate itself is not directly measurable from data. Instead, the variance of the isostable coordinates will be related to measured APDs, i.e., the time that the cell remains depolarized during a given action potential. The APD is a commonly used measurement to characterize the behavior of experimental cardiomyocytes. As in Figure 4, let t_1^m (resp. t_2^m) denote the time that the transmembrane voltage crosses some threshold Π with positive (resp. negative) slope during the m^{th} action potential. The m^{th} action potential duration is then defined as

$$T_{\text{APD}}^m = t_2^m - t_1^m. \tag{28}$$

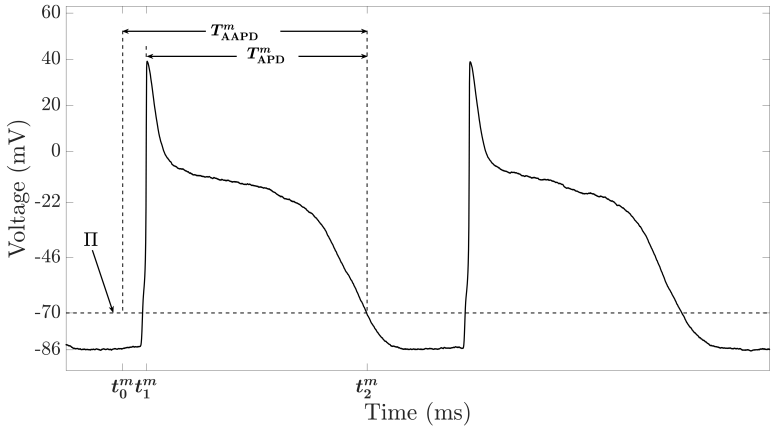

Figure 4: While the APD, defined in Equation (28) is a more natural experimental definition, both t_1^m and t_2^m are random variables, which would complicate the analysis below. By contrast, the AAPD defined in (29) consists of only one random variable (since t_0^m is deterministic). In practice, since $\text{var}(t_1^m - t_0^m)$ is small, the difference between the variance of the APDs and AAPDs is negligable. The voltage threshold, Π, defines a Poincaré section that is used to calculate APDs.

For simplicity of the exposition, we will consider an augmented action potential duration (AAPD) by defining t_0^m to be the moment that $\text{mod}(t, T_{\text{pace}}) = 0$ on the m^{th} cycle and letting

$$T_{\text{AAPD}}^m = t_2^m - t_0^m. \tag{29}$$

As illustrated in Figure 4, T_{AAPD}^m is slightly longer than T_{APD}^m. To proceed, we will use the operational phase reduced coordinate framework [52] to relate the time of crossing of a particular isochron to the time at which a trajectory crosses a specified Poincaré section. For the moment, consider the entrained periodic orbit of (2) that emerges when taking $u(t) = 0$. We will define $\tilde{t}_2^m$ to be the time that Π is crossed on the APD downstroke when $\psi = 0$ (i.e., the time that the APD would end if the system state is exactly on the limit cycle). We also recall that $\theta = \text{mod}(2\pi t/T, 2\pi)$ and define $\tilde{\theta}_2 \equiv \text{mod}(2\pi\tilde{t}_2^m/T, 2\pi)$ to be the corresponding phase when this crossing occurs. Note

that $\tilde{\theta}_2$ is the same from cycle-to-cycle. With this information, according to Equation (15) from [52], for $\mathcal{O}(\epsilon)$ values of ψ,

$$t_2^m = \tilde{t}_2^m - \frac{\psi(\tilde{t}_2^m) g^V(\tilde{\theta}_2)}{\dot{V}(\tilde{\theta}_2)} + \mathcal{O}(\epsilon^2), \tag{30}$$

where, as described in [52], $g^V(\theta)$ is the transmembrane voltage component of the Floquet eigenfunction associated with ψ, and $\dot{V}(\theta)$ is the time derivative of the transmembrane voltage evaluated on the unperturbed periodic orbit. Substituting Equation (30) into (29) and taking the variance to leading order yields

$$\begin{aligned}
\mathrm{var}(T^m_{\mathrm{AAPD}}) &= \mathrm{var}\left(\tilde{t}_2^m - \frac{\psi(\tilde{t}_2^m) g^V(\tilde{\theta}_2)}{\dot{V}(\tilde{\theta}_2)} - t_0^m \right) \\
&= \mathrm{var}\left(-\frac{\psi(\tilde{t}_2^m) g^V(\tilde{\theta}_2)}{\dot{V}(\tilde{\theta}_2)} \right) \\
&= \left(g^V(\tilde{\theta}_2)/\dot{V}(\tilde{\theta}_2) \right)^2 \mathrm{var}(\psi(\tilde{t}_2^m)),
\end{aligned} \tag{31}$$

where the second and third lines follow from the fact that $(\tilde{t}_2^m - t_0^m)$ and $g^V(\tilde{\theta}_2)/\dot{V}(\tilde{\theta}_2)$ are both constants. The time at which the variance of the isostable coordinates are evaluated in Equation (26) is arbitrary as long as it is consistent on a cycle-by-cycle basis. Therefore, taking $t = \tilde{t}_2^m$ in (26), starting with (31) one can write

$$\begin{aligned}
\mathrm{var}(T^*_{\mathrm{AAPD}}) - \mathrm{var}(T_{\mathrm{AAPD}}) &= \frac{\alpha\beta}{2} \left(\frac{g^V(\tilde{\theta}_2)}{\dot{V}(\tilde{\theta}_2)} \right)^2 b_n + \mathcal{O}(\alpha^2) \\
&= \alpha\mu b_n + \mathcal{O}(\alpha^2),
\end{aligned} \tag{32}$$

where T^*_{AAPD} (resp., T_{AAPD}) represent the augmented action potentials measured with (resp., without) input from $u(t)$ and $\mu = \beta(g^V(\tilde{\theta}_2)/\dot{V}(\tilde{\theta}_2))^2/2$. Here, it is assumed that $g^V(\theta)$ and $\dot{V}(\theta)$ only change by order α when the $\mathcal{O}(\alpha)$ input $u(t)$ is applied yielding the additional $\mathcal{O}(\alpha)$ terms in (32). Note that the integrand that determines β is strictly positive so that $\mu > 0$.

Finally, one can write rewrite the terms each AAPD as

$$\begin{aligned}
T^m_{\mathrm{AAPD}} &= t_2^m - t_0^m \\
&= t_2^m - t_1^m + t_1^m - t_0^m \\
&= T^m_{\mathrm{APD}} + t_1^m - t_0^m.
\end{aligned} \tag{33}$$

On each cycle $t_1^m - t_0^m$ is primarily a function of the pacing used to elicit action potentials, which does not change on a cycle-to-cycle basis. Consequently, the variance in the measurements of $t_1^m - t_0^m$ will generally be negligible compared to the variance of the APDs. For example, for simulations of (1) using the Noble model [32] $\mathrm{var}(t_1 - t_0)$ is more than 10,000 times smaller than the variance of the resulting APDs. Thus, it is generally possible to use the standard definition of the APD in Equation (32) instead of the AAPDs, that is,

$$\mathrm{var}(T^*_{\mathrm{APD}}) - \mathrm{var}(T_{\mathrm{APD}}) = \alpha\mu b_n + \mathcal{O}(\alpha^2). \tag{34}$$

3.4 Inference of Necessary Terms for Weakly Unstable Periodic Orbits

In order for the integrals from (25) to converge, the underlying periodic orbit must be stable so that κ is negative. However, for the application considered in this work of stabilizing an unstable

period-1 orbit, it is necessary to identify $C(\theta)$ when $\kappa > 0$. As shown here, supposing $\kappa > 0$ and small enough in magnitude so that it can be stabilized with a periodic input, the relationships derived in Section 3.2 can still be applied to estimate $C(\theta)$.

To begin, consider an unstable T-periodic orbit $y^\gamma(t)$ of (2) that exists when $u(t) = 0$. Taking $n_1 \in \mathbb{N}$, suppose that under the application of an input $u_1(t) = \alpha_1 \sin(2\pi n_1 t/T)$ that the resulting entrained orbit can be stabilized. Suppose also that under the application of a different input $u_2(t) = \alpha_1 \sin(2\pi n_1 t/T) + \alpha_2 \sin(2\pi n_2 t/T)$ where $n_2 \in \mathbb{N}$ that the resulting entrained orbit is still stabilized. Once again, it will be assumed that noise $\epsilon\eta(t)$ present in simulations of the reduced order equations. Letting $\text{var}(\psi_i^*)$ be the variance of the noisy isostable coordinate measurements and $\Delta\kappa_i$ and $\Delta I_i(\theta)$ be the terms of the shifted orbit under the application of the inputs $u_i(t)$ for $i = 1, 2$, from (24) we have

$$\begin{aligned}\text{var}(\psi_2^*) - \text{var}(\psi_1^*) = \epsilon^2 \int_{t_0}^{t} e^{2(\kappa+\Delta\kappa_2)(t-s)}(I(\omega s) + \Delta I_2(\omega s))^2 ds \\ - \epsilon^2 \int_{t_0}^{t} e^{2(\kappa+\Delta\kappa_1)(t-s)}(I(\omega s) + \Delta I_1(\omega s))^2 ds. \end{aligned} \tag{35}$$

Above, because the shifted orbits are now stable, both $\kappa + \Delta\kappa_1$ and $\kappa + \Delta\kappa_2$ are less than zero so that the integrals (35) converge as t approaches infinity.

Following the derivation from Section 3.2, assuming that α_1 and α_2 are small, to leading order, one can write (35) as

$$\text{var}(\psi_2^*) - \text{var}(\psi_1^*) = (\Delta\kappa_2 - \Delta\kappa_1)\beta + 2\epsilon^2 \int_{t_0}^{t} \left[e^{2\kappa(t-s)} I(\omega s) I'(\omega s)(\Delta I_2(\omega s) - \Delta I_1(\omega s)) \right] ds. \tag{36}$$

As explained in Section 3.2, the remaining integral in (36) is negligibly small relative to $(\kappa_1 - \kappa_2)\beta$ and can be ignored. Finally, substituting (7) into the remaining terms of (36) and simplifying yields

$$\begin{aligned}\text{var}(\psi_2^*) - \text{var}(\psi_1^*) &= \frac{\alpha_2 \beta}{T} \int_0^T C(\omega t) \sin(2\pi n_2 t/T) dt \\ &= \frac{\alpha_2 \beta}{2} b_n, \end{aligned} \tag{37}$$

where b_n is the n^{th} term of the Fourier series expansion of $C(\omega t)$. Once again, an identical argument can be used to obtain cosine terms of the Fourier series expansion. Note the similarity between (37) and (26). Provided that both $u_1(t)$ and $u_2(t)$ stabilize the weakly unstable periodic orbit, the differences in the variance of the resulting isostable coordinates can be used to infer the terms of the Fourier series expansion of $C(\theta)$. Similar to (34) it is possible to use direct measurements of the APDs instead of measurements of the isostable coordinates so that to leading order, Equation (37) becomes

$$\text{var}(T^*_{\text{APD}_2}) - \text{var}(T^*_{\text{APD}_1}) = \alpha_2 \mu b_n, \tag{38}$$

where $\text{var}(T^*_{\text{APD}_1})$ and $\text{var}(T^*_{\text{APD}_2})$ correspond to the resulting variances measured when $u_1(t)$ and $u_2(t)$ are applied, respectively.

3.5 Procedure to Infer the Terms of the Fourier Series expansion of $C(\theta)$ for Cardiomyocytes

Combining the results 3.2-3.4, consider a a T-periodic, entrained orbit describing excitable cardiomyocytes that can be represented according to (2). One can infer $\mu C(\theta)$, where $\mu > 0$ is an unknown constant, for the reduced order Equation (6) using the procedure detailed below.

3.5.1 Implementation for a Stable Entrained Orbit

Step 1) Simulate (2) with $u = 0$. Measure every m^{th} APD where m is chosen so that the individual measurements are well-approximated as independent to each other. Compute the resulting variance of the collection of measurements.

Step 2) Repeat Step 1 using $u(t) = \alpha \sin(2\pi t/T)$.

Step 3) Comparing the resulting variance in APDs from Step 2 to the variance obtained from Step 1, it is possible to infer the scaled Fourier coefficients μb_1 from (34) where μ is an unknown positive constant.

Step 4) Repeat Steps 2 and 3 taking $u(t) = \alpha \sin(4\pi t/T), \alpha \sin(6\pi t/T) \dots$ and $u(t) = \alpha, \alpha \cos(2\pi t/T)$, $\alpha \cos(4\pi t/T) \dots$ to obtain the scaled Fourier coefficients μb_n and μa_n using the relations of the form (34).

3.5.2 Implementation for a Weakly Unstable Entrained Orbit

Step 1) Simulate (2) with $u_1(t) = \alpha_1 \sin(2\pi n_1 t/T)$. The magnitude and frequency of $u_1(t)$ must be chosen so that it stabilizes the unstable periodic orbit. After initial transient behavior decays, measure every m^{th} APD where m is chosen so that the individual measurements are well-approximated as independent to each other. Compute the resulting variance of the collection of measurements.

Step 2) Repeat Step 1 using $u_2(t) = \alpha_2 \sin(2\pi t/T) + u_1(t)$.

Step 3) Comparing the resulting variance in APDs from Step 2 to the variance obtained from Step 1, it is possible to infer the scaled Fourier coefficients μb_1 from (34) where μ is an unknown positive constant.

Step 4) Repeat Steps 2 and 3 taking $u_2(t) = \alpha_2 \sin(4\pi t/T) + u_1(t), \alpha_2 \sin(6\pi t/T) + u_1(t) \dots$ and $u_2(t) = \alpha_2 + u_1(t), \alpha_2 \cos(2\pi t/T) + u_1(t), \alpha_2 \cos(4\pi t/T) + u_1(t) \dots$ to obtain the scaled Fourier coefficients μb_n and μa_n using the relations or the form (38).

From an experimental perspective, the strategy suggested above is attractive because of its simplicity – it only requires the ability to measure a series of APDs and information about $C(\theta)$ can be inferred by computing the variance of the resulting measurements. One drawback, however, is that μ is generally unknown so that the shape of $C(\theta)$ but not the magnitude can be obtained. Nevertheless, as we will see in the examples to follow, knowledge of the shape of $C(\theta)$ alone is sufficient to implement the proposed optimal nonfeedback control strategies from Section 3.1 for eliminating alternans.

4 Results

As discussed in Section 3.1, an energy-optimal strategy for eliminating alternans using periodic stimulation can be implemented solely with knowledge of $C(\theta)$ from (6), i.e., that capture the second order accurate terms of the isostable dynamics. Here we apply the strategies developed in the previous section to infer the function $C(\theta)$ with a data-driven strategy. This technique is then leveraged to identify energy-optimal periodic stimuli that can stabilize unstable period-1 solutions thereby eliminating alternans using the optimal control framework in Section 3.1.

4.1 Implementation of the Proposed Techniques for a Stable Periodic Orbit

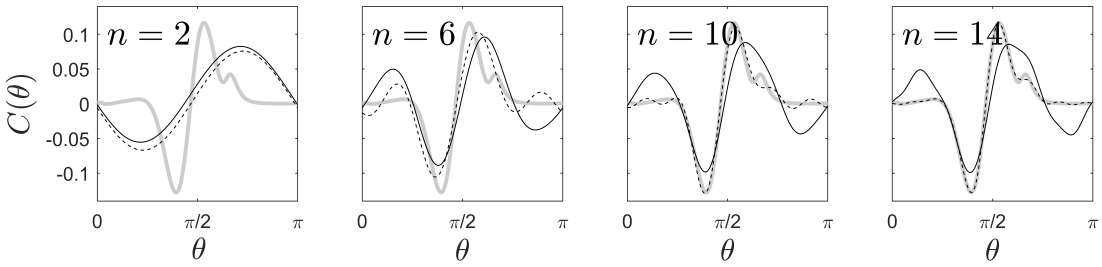

Figure 5: Illustration of the proposed strategy for estimating $C(\theta)$ of the reduced Equation (6) for a stable entrained orbit. The grey lines in each panel show the exact value of $C(\theta)$ calculated directly from the model equations using methods described in [47]. Black lines in each panel show the data-driven approximation of $C(\theta)/\mu = a_0/2 + \sum_{k=0}^{n} (b_k \sin(2\pi kt/T) + a_n \cos(2\pi kt/T))$ for the indicated value of n. The coefficients of the Fourier series expansion are determined using the strategy detailed in Section 3.5.1. Dashed lines show the first n Fourier modes of the exact solution The magnitudes of the resulting plots are appropriately normalized to provide visual comparisons with the exact solutions. While the proposed estimation strategy is unable to capture all of the detailed associated with the high frequency modes, the contributions of the lower frequency modes are accurately estimated.

We consider the Noble model equations given in Equation (A1) taking $T_{\text{pace}} = 330$ ms with $\epsilon = 0.14$. After allowing initial transients to decay, a representative plot of the resulting stable Period-1 waveform is shown in panel (A) of Figure 1. As discussed in Appendix B, because the principle Floquet multiplier is negative, when taking $T = 2T_{\text{pace}}$, $C(\theta)$ is periodic with period T_{pace}. Consequently, all odd coefficients of the Fourier series expansion (27) are simply zero. Following the procedure detailed in Section 3.5.1, separate trials taking inputs of the form $u(t) = 0.3\sin(2n\pi t/T)$ and $u(t) = 0.3\sin(2n\pi t/T)$ are performed for all even $n \leq 14$. For each trial, the associated input is applied for approximately 5000 cycles and the variance of the resulting APDs is measured. A large number of cycles is considered here so that the estimates of each Fourier coefficient do not change significantly when the procedure is repeated, however, accurate results can still be obtained using fewer measurements as will be illustrated in the results from Section 4.2. These measurements are then used to infer $\mu C(\theta)$ where $\mu > 0$ is an undetermined constant as defined below Equation (32). In Figure 5, plots of the resulting curves are shown highlighting accuracy of the proposed method. The accuracy in the estimate of $C(\theta)$ increases as more terms are included, however, diminishing returns are observed with n larger than 6 in this example.

While the proposed estimation strategy accurately captures the lower frequency modes, the higher frequency modes (i.e., those with $n > 6$) are not accurately inferred. This is likely due to the fact that the magnitudes of these high frequency terms contributing to $C(\theta)$ are relatively small, and as such, it is hard to detect their influence on the APDs. As will be shown in the examples to follow, because these higher frequency modes have a relatively small contribution to the overall value of $C(\theta)$, these errors do not significantly degrade the accuracy of the resulting reduced order models.

4.2 Implementation of Proposed Techniques for an Unstable Periodic Orbit

In this example, we consider the data-driven inference of $C(\theta)$ for an unstable period-1 orbit and the subsequent design of a control input to eliminate alternans. Once again, we consider the Noble model equations from (A1), this time pacing at a rate of $T_{\text{pace}} = 253$ ms. The period-1 solution is unstable at this pacing rate; the Floquet multiplier corresponding to a single action potential is -1.05. When taking $T = 2T_{\text{pace}}$ the resulting Floquet exponent is 1.98×10^{-4}.

In numerical simulations of (1) we choose the $\epsilon = 0.20$ to set the noise strength. Because the period-1 orbit is unstable, alternans emerge in steady state in the absence of any external input. Panel (B) of Figure 6 show histograms of the resulting APDs collected for over 8000 representative action potentials. In steady state, action potential durations alternate between about 130 and 230 ms. These times correspond to peaks on the corresponding histogram. Occasionally, after a long action potential, the next action potential will fail to initiate. In tissue, such failure to initiate can cause conduction block that creates favorable conditions for the genesis of reentrant arrhythimas associated with fibrillation [31], [7]. After a failed action potential, the subsequent APD is approximately 360 ms. These occurrences account for a small but nonnegligible portion of the observed APDs.

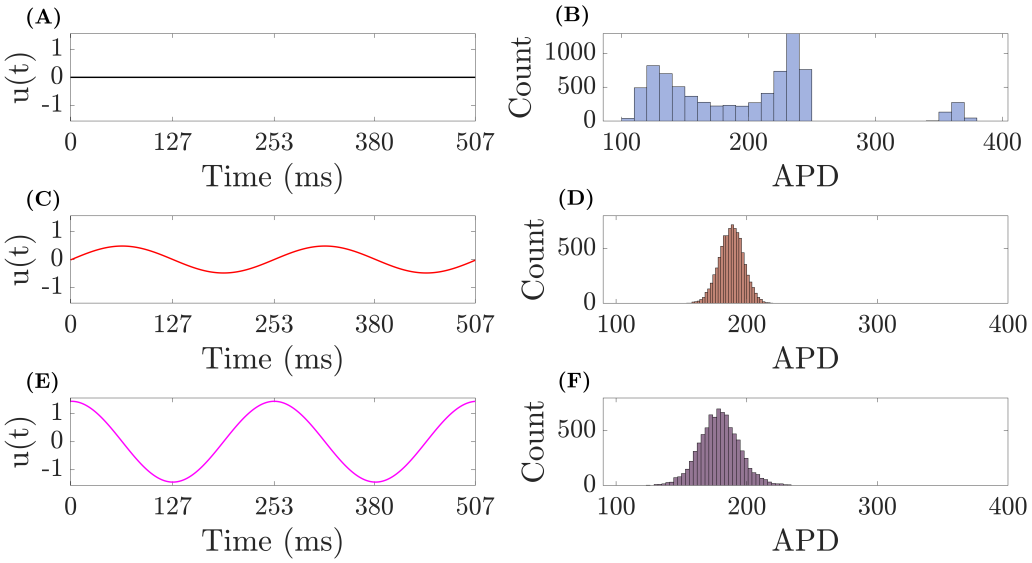

Figure 6: Various periodic inputs $u(t)$ (in μA/cm^2) are applied (panels A,C,E) to the Noble model from Equation (A1) using a pacing rate of 253 ms. When no input is applied, alternans emerges in steady state as seen in the histogram in panel (B). Occasionally, after a particularly large action potential duration, the ensuing action potential fails, leading to an APD of approximately 350 ms immediately afterward. The application of the sinusoidal inputs in panels (C) and (E) stabilize the unstable period-1 alternans-free orbit, thereby eliminating alternans as can be seen in corresponding panels (D) and (F), respectively.

As discussed in Section 3.4, in order to infer the reduced order terms associated with the unstable, period-1 alternans free solution, it is necessary to find some nominal input that eliminates alternans. Panels (C) and (D) of Figure 6 show examples of such stimuli that are proportional to $\sin(4\pi t/T)$ and $\cos(4\pi t/T)$, respectively. The corresponding histograms in panels (D) and (F)

indicate that alternans is eliminated and either of these stimuli can be used as the necessary stabilizing input $u_1(t)$ to implement the strategy for identifying $C(\theta)$ using the procedure described in Section 3.5.2. Figure 7 illustrates the results of implementing this procedure. Inputs $u_2(t)$ are shown as colored traces in panels (A) and (C) and are applied in addition to the baseline inputs $u_1(t)$ shown in grey. Histograms of of the measured action potentials of corresponding color are shown in panels (B) and (D).

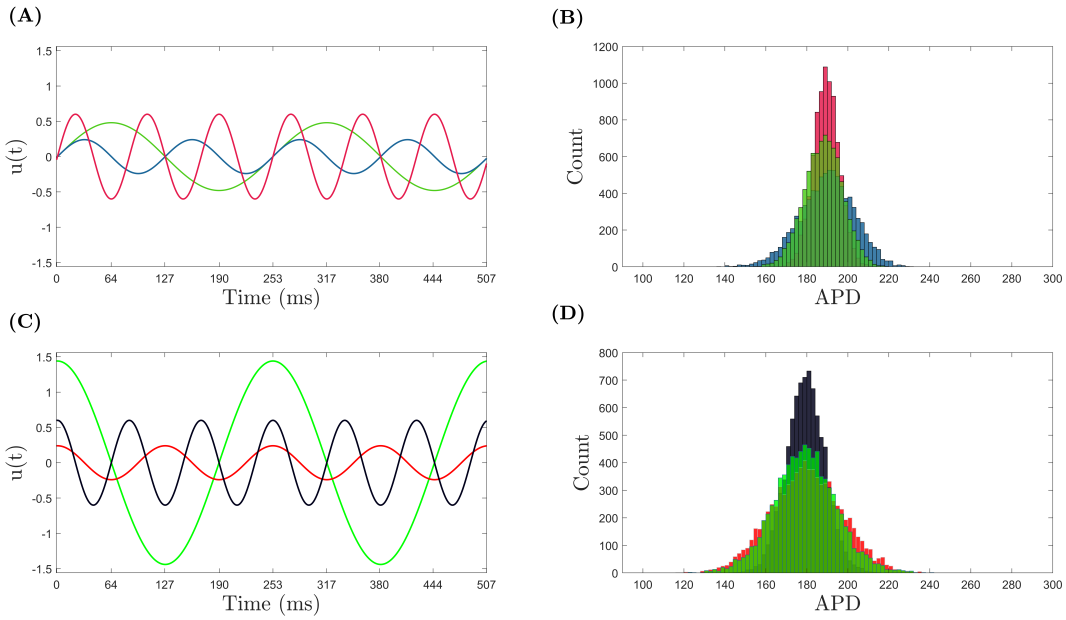

Figure 7: Green lines in panels (A) and (C) represent the baseline stabilizing stimulus $u_1(t)$ (in μA/cm^2) as described in the procedure from Section 3.5.2. Green bars in panels (B) and (D) show the respective histograms of the APDs. Black, red, and blue lines in panels (A) and (C) show stimuli $u_2(t)-u_1(t)$, highlighting the additional inputs added to $u_1(t)$. Histograms of corresponding color are shown in panels (B) and (D). Differences between the resulting variances of the measured action potentials are then used to infer information about the shape of $C(\theta)$.

The variances of the measured APDs from Figure 7 are used as part of the procedure from Section 3.5.2 to infer the shape of $C(\theta)$. In order to investigate the number of APDs necessary to obtain an accurate estimate of the curve $C(\theta)$, the fitting procedure is repeated over multiple independent trials that measure different numbers APDs. These results are shown in Figure 8. While accurate estimates can be obtained when using a small number of APDs, the variation in the inferred curves tends to diminish when more APDs are measured. Additionally, as more Fourier modes are estimated, the accuracy of the resulting approximation improves. Reduced order curves obtained from trials taking 8000 APDs with various choices of n are used to identify the shape of energy-optimal stimuli for stabilizing the period-1 alternans-free solution with the strategy described in Section 3.1. Specifically, as shown by Equation (14), the optimal stabilizing stimulus is proportional to $-C(\theta)$. In order to provide an estimate of the stabilization efficiency for each resulting input, the resulting optimal $u(t)$ is applied to the full model (1) using the pacing rate $T_{\text{pace}} = 253$ ms. The magnitude is adjusted until alternans is eliminated and the resulting variance of the action potentials is between 65 and 67 ms. The resulting variance in the action potentials

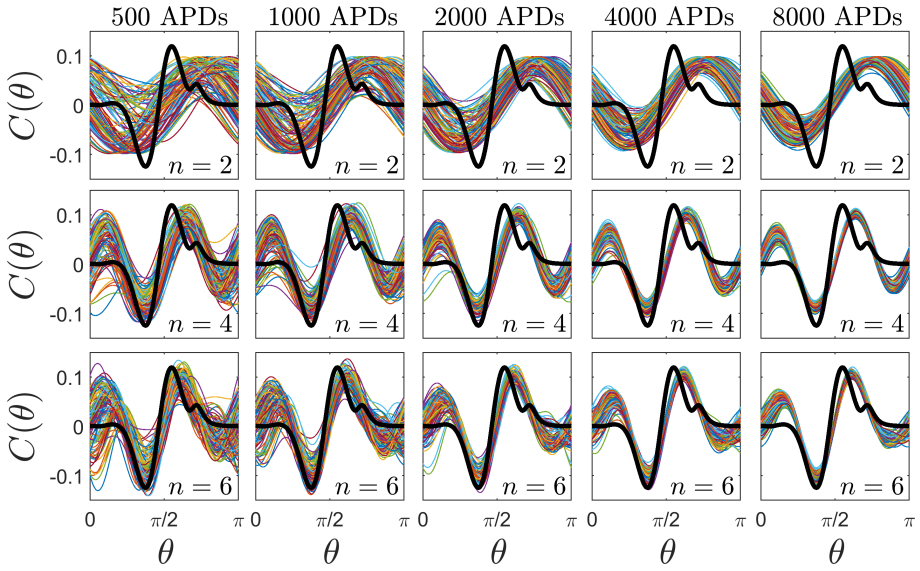

Figure 8: Results from implementing the proposed strategy from Section 3.5.2 for estimating $C(\theta)$ from the reduced equations of the form (6) associated with an unstable periodic orbit. Each panel shows 100 independent estimates of $C(\theta)$ (colored lines) using the indicated number of APDs to estimate the required APD variances according to the Fourier series expansion $C(\theta)/\mu = a_0/2 + \sum_{k=0}^{n} (b_k \sin(2\pi kt/T) + a_n \cos(2\pi kt/T))$. The magnitudes of the resulting plots are appropriately normalized to provide visual comparisons with the exact solutions. The black lines in each panel show the exact value of $C(\theta)$ calculated numerically from the model equations using methods described in [47]. Taking more terms of the Fourier series expansion (i.e., with n larger than 6) only yields small differences in the resulting values of $C(\theta)$ and these results are not shown.

is proportional to the effective Floquet exponent (as illustrated by Equation (25)). Therefore, by mandating the same variance for each stabilizing stimulus, we can gauge the efficiency by considering $\int_0^{T_{\text{pace}}} u^2(t)dt$ for each stimulus. These results are shown in Figure 9. In general, estimating more terms of the Fourier series expansion of $C(\theta)$ will yield inputs that are closer to optimal, however, diminishing returns are observed for the higher order coefficients.

We are unaware of other nonfeedback control strategies that could be used to stabilize alternans. Nevertheless, in order to make comparisons between other previously considered alternans elimination strategies, we consider delayed feedback control of the form [35]

$$u(t) = \gamma(V(t) - V(t - \tau)), \tag{39}$$

where $\tau = T_{\text{pace}}$ and γ is a constant. The general delayed feedback control framework has been widely studied as a means of stabilizing unstable periodic orbits [40], [9] and has also been previously investigated in terms of its ability to control cardiac alternans [37]. In contrast to the proposed nonfeedback control strategy, the delayed feedback control requires the ability to continuously and accurately measure the transmembrane voltage while concurrently applying input. Using $\gamma = -0.025$, we find that the delayed feedback strategy (39) is able to eliminate alternans using approximately 76 percent less energy than the nonfeedback control strategy as shown in Figure 9. Qualitatively similar results are obtained using values of γ between -0.01 and -0.05. While the delayed feedback strategy uses less overall energy, from a practical standpoint it can be difficult to simultaneously apply input and take measurements from the same probe. Additionally, mea-

surement noise and other uncertainties can lead to errors that degrade the effectiveness of such feedback control methods [2], [40]; these practical considerations are not investigated here.

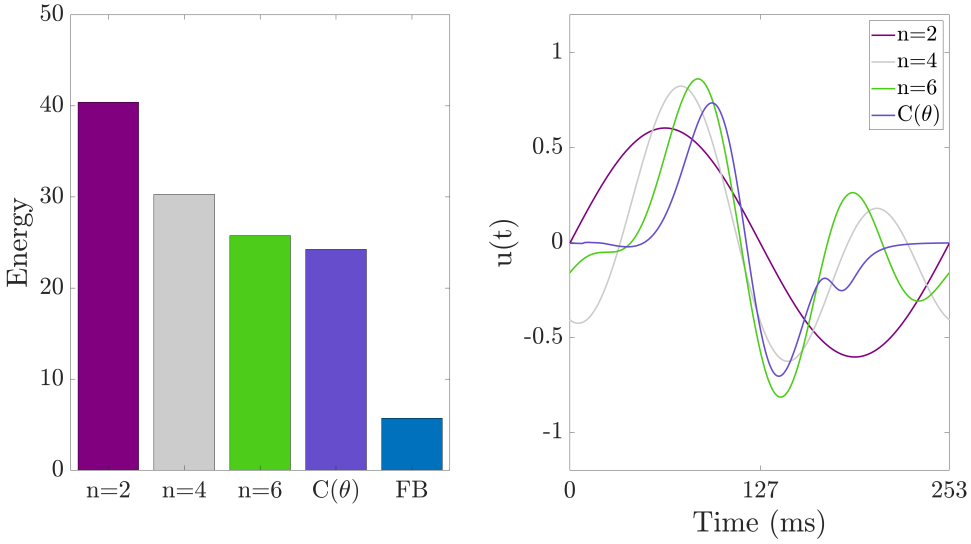

Figure 9: Using the proposed strategy to infer the curve $C(\theta)$ with Fourier modes up to the indicated value of n (and also using the exact value of $C(\theta)$), the right panel shows the resulting optimal stimulus (in μA/cm^2) that stabilizes alternans and yields a variance of 66 ± 1 ms in the APDs. Corresponding bars in the left panel represent value of $\int_0^{T_{\text{pace}}} u^2(t)dt$ for the indicated stimuli. Resulting energy consumption using the feedback (FB) control strategy from (39) taking $\gamma = -0.025$ is also shown, where the reported energy usage represents the average per pacing cycle. The input using the true value of $C(\theta)$ is optimal when using the nonfeedback strategy and the approximations that result when using the inferred curves provide better estimates of the optimal inputs as more terms of the Fourier series expansion are included. While the delayed feedback control uses less energy than the proposed nonfeedback strategy, practical drawbacks associated with the implementation of feedback control in experimental situations may outweigh the benefit from the energy savings. As such, the delayed feedback control strategy and the nonfeedback control strategy cannot be directly compared solely on the basis of overall energy usage.

5 Conclusion

Phase-isostable reduction frameworks represent a powerful model reduction strategy that can accurately replicate system dynamics in situations where first order accurate techniques alone are unable to capture the perturbed system behavior. While many strategies are available to numerically compute the reduced order terms to high orders of accuracy when the model equations are known [47], [53], [50], fewer options are available to infer the necessary terms of the reduction solely from observed data, for example, when the model equations themselves are unknown. Methods akin to the 'direct method' [19], [10] can be used to approximate $Z(\theta)$ and $I(\theta)$ from Equations (3) and (4) from experimental data. However, there are currently no general techniques that can be used to estimate $B(\theta)$ and $C(\theta)$, i.e., the higher order terms that characterize dominant system nonlinearities.

In this work, we investigate the behavior of noisy oscillations that are entrained to an external input which admit reduced order models of the form (6). By analyzing the variance of the measured isostable coordinates on a cycle-by-cycle basis in response to additive white noise, we are able to develop a procedure to estimate the function $C(\theta)$. Furthermore, we find that this knowledge of $C(\theta)$ ultimately allows for the identification of energy-optimal nonfeedback control inputs for eliminating cardiac alternans that shift Floquet exponents of associated unstable period-1 orbits from positive to negative values. As implemented in this work, this strategy does not consider the estimation of the other terms from the phase amplitude reduced equations (3) and (4), but could be used in conjunction with other data driven strategies such as those suggested in [49] or [53] to get a fuller picture of the phase and isostable dynamics. It would be of interest in future work to extend the proposed model inference techniques for reduced order systems that require more than one isostable coordinate. Additionally, incorporating higher order noise terms such as the Ito correction [11] may allow for more accurate inference of the high frequency Fourier modes.

From the perspective of eliminating cardiac alternans, there are many limitations that this work does not address. Foremost, the Noble model [32] used here is relatively simple and only contains a limited description of the underlying cellular currents. While the data-driven model inference strategy proposed here does not depend on the specific model used, it would be interesting to investigate its utility in more complicated cardiac models. Additionally, while the work presented here focuses on the elimination of alternans in a single cell, the true danger of alternans is in the dispersion of refractoriness it can induce in tissue. This phenomenon is generally referred to as discordant alternans and can emerge due to conduction velocity restitution and other factors [44], [36], [23]. These effects are not considered in this work, but it would be of interest to adapt the methods presented here for partial differential equation models of cardiac action potential propagation where stabilization of the unstable dynamics that give rise to concordant and discordant alternans can be investigated. Additionally, the present study considers direct transmembrane charge injection as the control input for eliminating alternans. While this is possible in experimental preparations, it would be more feasible to consider other inputs such as the application of a time-varying extracellular voltage gradient (which would need to be considered with a bidomain model [43]). These considerations will be addressed in future work.

Importantly, this work highlights that noise, which is generally present in most biological systems, can be exploited in order to identify nonlinear terms associated with reduced order models. Further investigation could yield other strategies for robust identification of reduced order dynamical models in noisy environments.

This material is based upon the work supported by the National Science Foundation (NSF) under Grant No. CMMI-1933583.

Appendix A Noble Model Equations

The Noble model equations from [32] are used in numerical simulations in this work. The model equations are reproduced below:

$$\begin{aligned} C_m\dot{V} &= i_{Na} + i_K + i_{An} + \alpha u(t) + \epsilon\eta(t), \\ \dot{m} &= \alpha_m(1-m) - \beta_m m, \\ \dot{h} &= \alpha_h(1-h) - \beta_h h, \\ \dot{n} &= \alpha_n(1-n) - \beta_n n. \end{aligned} \tag{A1}$$

Here, V is the transmembrane voltage and m, h, and n are gating variables that set the value of the various ionic currents. $C_m = 12\mu\text{F/cm}^2$ is the membrane capacitance, $\eta(t)$ represents independent and identically distributed zero mean white noise with unit intensity, ϵ and α are small constant parameters, and $u(t)$ is an external input. Relationships governing the ionic currents are

$$\begin{aligned} i_{Na} &= (400m^3h + 0.132)(V - 40), \\ i_K &= (1.2n^4 + 1.2\exp((-V - 90)/50) + 0.015\exp((V + 90)/60))(V + 100), \\ i_{An} &= g_{an}(V + 60), \end{aligned} \tag{A2}$$

where g_{an} is a variable leak conductance that is chosen to be 0 in this work. Additional coefficients are given by

$$\begin{aligned} \alpha_m &= \frac{100(-V - 48)}{\exp((-V - 48)/15) - 1}, \\ \beta_m &= \frac{120(V + 8)}{\exp((V + 8)/5) - 1}, \\ \alpha_h &= 170\exp((-V - 90)/20), \\ \beta_h &= \frac{1000}{1 + \exp((-V - 42)/10)}, \\ \alpha_n &= \frac{0.1(-V - 50)}{\exp((-V - 50)/10) - 1}, \\ \beta_n &= 2\exp((-V - 90)/80). \end{aligned} \tag{A3}$$

Appendix B Characteristics of the Phase-Isostable Reduction For Systems With Negative Floquet Multipliers

The problem of eliminating alternans in cardiac models of the form (2) can be viewed from a dynamical systems perspective as stabilizing an alternans-free periodic-1 orbit that loses stability as a result of a period doubling bifurcation. As explained in the main text, this orbit (with period T_{pace}) loses stability as its principle Floquet multiplier λ, crosses from $\lambda > -1$ to $\lambda < -1$. Because this Floquet multipler is negative, we let two action potentials comprise the full periodic orbit so that $T = 2T_{\text{pace}}$ in the isostable reduction yielding a positive principle Floquet multiplier. Here, we show that in this situation, $I(\theta + \pi) = -I(\theta)$ and that $C(\theta + \pi) = C(\theta)$ for the reduced order equations (6).

To begin, consider a general dynamical system of the form

$$\dot{x} = F(x), \tag{B1}$$

where $x \in \mathbb{R}^N$ and F gives the system dynamics. Suppose that (B1) admits a T_{pace}-periodic orbit $x^\gamma(t)$. Letting $\Delta x = x - x^\gamma(t)$ be a small perturbation from the periodic orbit, one can linearize with respect to the periodic orbit to find

$$\Delta\dot{x} = J(x^\gamma(t))\Delta x, \tag{B2}$$

where $J(x^\gamma(t))$ is the Jacobian evaluated at $x^\gamma(t)$. Let $\Phi(t, t_0)$ be the state transition matrix associated with (B2) with the property that $x(T_{\text{pace}}) = \Phi(T_{\text{pace}}, 0)x(0)$. As stated in the main

text, we assume that $|\lambda|$ close to 1 so that it decays slowly and that all other nonunity Floquet multipliers (i.e., the eigenvalues of $\Phi(T_{\text{pace}}, 0)$) are close to 0 so that they can be ignored. When considering a period of $T = 2T_{\text{pace}}$, $\kappa = \frac{\log(\lambda^2)}{2T_{\text{pace}}}$. Letting T be the overall period used in in the phase-isostable reduction framework, from [50], we know that $I(t)$ is the T-periodic solution to

$$\frac{dI}{dt} = (\kappa \text{Id} - J^T(x^\gamma(t))I(t), \tag{B3}$$

where Id is an appropriately sized identity matrix. The adjoint system of (B2) is

$$\dot{y} = -J^T(x^\gamma(t))y, \tag{B4}$$

and the solution to this differential equation is given by $y(T_{\text{pace}}) = \Phi^T(0, T_{\text{pace}})y(0) = (\Phi^T(T_{\text{pace}}, 0))^{-1}y(0)$ so that $1/\lambda$ is an eigenvalue of $\Phi^T(0, T_{\text{pace}})$. Let $\tilde{y}(t)$ be the solution to (B4) for which $\tilde{y}(T_{\text{pace}}) = (1/\lambda)\tilde{y}(0)$. Through direct substitution, one can verify that $I(t) = \tilde{y}(t)\exp(\kappa t)$ is the T-periodic solution to (B3). With this in mind, one finds

$$\begin{aligned} I(T_{\text{pace}} + t) &= \tilde{y}(T_{\text{pace}} + t)\exp(\kappa(T_{\text{pace}} + t)) \\ &= \Phi^T(0, t)\Phi^T(0, T_{\text{pace}})\tilde{y}(0)\exp(\kappa t)\exp(\kappa T_{\text{pace}}) \\ &= -\Phi^T(0, t)\tilde{y}(0)\exp(\kappa t) \\ &= -I(t). \end{aligned} \tag{B5}$$

In order to determine $C(\theta)$, it will be necessary to compute the Floquet eigenfunction, $g(\theta)$, corresponding to κ. As discussed in [50], $g(\theta(t))$ is the T-periodic solution to

$$\frac{dg}{dt} = (J(x^\gamma(t)) - \kappa \text{Id})g(t). \tag{B6}$$

Letting $\Delta\tilde{x}(t)$ be the solution to (B2) for which $\Delta\tilde{x}(T_{\text{pace}}) = \lambda\Delta\tilde{x}(0)$, one can verify that $g(t) = \Delta\tilde{x}(t)\exp(-\kappa t)$ is the T-periodic solution to (B6) through direct substitution. Once again, with this in mind, one finds

$$\begin{aligned} g(T_{\text{pace}} + t) &= \Delta\tilde{x}(T_{\text{pace}} + t)\exp(-\kappa(T_{\text{pace}} + t)) \\ &= \Phi(t, 0)\Phi(T_{\text{pace}}, 0)\Delta\tilde{x}(0)\exp(-\kappa t)\exp(-\kappa T_{\text{pace}}) \\ &= -\Phi(0, t)\Delta\tilde{x}(0)\exp(-\kappa t) \\ &= -g(t). \end{aligned} \tag{B7}$$

From [50], $C(t)$ can be obtained by computing the T-periodic solution to the linear time-varying system

$$\begin{aligned} \frac{dC(t)}{dt} &= -\sum_{i=1}^{N}\left[I^i(t)H_{i,x^\gamma(t)}g(t)\right] - J^T(x^\gamma(t))C(t) \\ &= -J^T(x^\gamma(t))C(t) + D(t), \end{aligned} \tag{B8}$$

where $I^i(t) \equiv e_i^T I(t)$ with e_i being the i^{th} component of the standard basis, $H_{i,x^\gamma(t)}$ is the Hessian matrix of the i^{th} component of F. The term $D(t) = -\sum_{i=1}^{N}\left[I^i(t)H_{i,x^\gamma(t)}g(t)\right]$ is a simplification that isolates the terms that comprise an effective time-varying input. Note that $D(t)$ is T_{pace}-periodic as can be seen after direct substitution of the relations (B5) and (B7). Recalling that the

state transition matrix from time t_0 to t for the equation $\dot{y} = -J^T(x^\gamma(t))y$ is given by $\Phi^T(t_0, t)$, the unique solution to (B8) is given by the variation of constants formula [17]

$$C(t) = \Phi^T(0,t)C(0) + \int_0^t \Phi^T(\tau,t)D(\tau)d\tau. \tag{B9}$$

Noting that $C(t)$ must be T-periodic, $C(0)$ must be an eigenvector associated with the unity Floquet multiplier of $\Phi^T(0, T_{\text{pace}})$ so that the term $\Phi^T(0,t)C(0)$ is T_{pace}-periodic. Also note that the integrand of (B9) is T_{pace}-periodic so that the entire solution $C(t)$ must also be T_{pace}-periodic. Finally, along the periodic orbit, $\theta = \omega t = 2\pi t/T = \pi t/T_{\text{pace}}$ and thus we find that $I(\theta+\pi) = -I(\theta)$ and that $C(\theta + \pi) = C(\theta)$ as desired.

Appendix C Characteristics of Phase-Isostable Reduced Equations for Unstable Entrained Orbits

Consider an unstable entrained periodic orbit described by (2) that emerges due to periodic forcing $I_{\text{ext}}(t)$. For convenience of notation, we let $y \equiv \begin{bmatrix} x & a \end{bmatrix}^T \in \mathbb{R}^{N+1}$ and let

$$G(y) \equiv \begin{bmatrix} F(x) + I_{\text{ext}}(a) \\ 1 \end{bmatrix} \in \mathbb{R}^{N+1} \tag{C1}$$

represent the noiseless, unperturbed dynamics. Here, F and I_{ext} are defined as part of (2). Let $y^\gamma(t)$ denote the unstable periodic orbit. As done in the main text, we assume that the neglected isostable coordinates have Floquet exponents that are negative and large in magnitude. We let $\kappa > 0$ be the unstable, nonneglected Floquet exponent. As explained in [48], a reduced order set of phase and isostable coordinates associated with this unstable orbit can be obtained with dynamics of the form (3) and (4) that are valid to leading order $|\Delta x|^2$, where $|\Delta x| \equiv x(t) - x^\gamma(t)$. The phase response curve $Z(\theta)$ can be obtained by identifying the periodic solution to the adjoint equation [3]

$$\frac{dZ}{dt} = -J^T(y^\gamma(t))Z, \tag{C2}$$

where J is the Jacobian of G evaluated at $y^\gamma(t)$ and $Z(t)$ is normalized so that $G^T(y(t))Z(t) = \omega$. Considering the structure of (2), the $N + 1^{\text{th}}$ column of $J^T(y^\gamma(t))$ contains only zeros. Therefore

$$Z(t) = \begin{bmatrix} 0 & 0 & \dots & 0 & \omega \end{bmatrix}^T \tag{C3}$$

is the appropriately normalized periodic solution to (C2). Furthermore, as detailed in [47], $B(t)$ is the periodic solution to

$$\frac{dB(t)}{dt} = -\sum_{i=1}^{N+1} \left[Z^i(t) H_{i,x^\gamma(t)} g(t) \right] - (J^T(x^\gamma(t)) + \kappa \text{Id})B(t), \tag{C4}$$

where $Z^i(t) \equiv e_i^T Z(t)$ with e_i being the i^{th} component of the standard basis, $H_{i,x^\gamma(t)}$ is the Hessian matrix of the i^{th} component of G, and $g(t)$ is defined above Equation (B6). From (C3), Z^i is 0 for $i = 1, \dots, N$. Furthermore, $H_{N+1,x^\gamma(t)} = 0$ as can be seen from (C1). The only periodic solution to (C3) is then $B(t) = \begin{bmatrix} 0 & 0 & \dots & 0 & 0 \end{bmatrix}^T$. Assuming that direct perturbations to a are not possible since it is a time-like variable, to leading order accuracy Equation (3) becomes $\dot{\theta} = \omega$ so that the phase dynamics can be eliminated and the reduced order dynamics take the form (5).

References

[1] H. Arbabi and I. Mezic. Ergodic theory, dynamic mode decomposition, and computation of spectral properties of the Koopman operator. *SIAM Journal on Applied Dynamical Systems*, 16(4):2096–2126, 2017.

[2] S. Boccaletti, C. Grebogi, Y. C. Lai, H. Mancini, and D. Maza. The control of chaos: theory and applications. *Physics Reports*, 329(3):103–197, 2000.

[3] E. Brown, J. Moehlis, and P. Holmes. On the phase reduction and response dynamics of neural oscillator populations. *Neural Computation*, 16(4):673–715, 2004.

[4] S. L. Brunton, B. W. Brunton, J. L. Proctor, E. Kaiser, and N. J. Kutz. Chaos as an intermittently forced linear system. *Nature Communications*, 8(1):1–9, 2017.

[5] M. Budišić, R. Mohr, and I. Mezić. Applied Koopmanism. *Chaos: An Interdisciplinary Journal of Nonlinear Science*, 22(4):047510, 2012.

[6] D. J. Christini, M. L. Riccio, C. A. Culianu, J. J. Fox, A. Karma, and R. F. Gilmour Jr. Control of electrical alternans in canine cardiac Purkinje fibers. *Physical Review Letters*, 96(10):104101, 2006.

[7] M. J. Cutler and D. S. Rosenbaum. Explaining the clinical manifestations of T wave alternans in patients at risk for sudden cardiac death. *Heart Rhythm*, 6(3):S22–S28, 2009.

[8] G. B. Ermentrout and D. H. Terman. *Mathematical Foundations of Neuroscience*, volume 35. Springer, New York, 2010.

[9] A. L. Fradkov and R. J. Evans. Control of chaos: Methods and applications in engineering. *Annual Reviews in Control*, 29(1):33–56, 2005.

[10] R. F. Galán, G. B. Ermentrout, and N. N. Urban. Efficient estimation of phase-resetting curves in real neurons and its significance for neural-network modeling. *Physical Review Letters*, 94(15):158101, 2005.

[11] C. W. Gardiner. *Handbook of Stochastic Methods: for Physics, Chemistry and the Natural Sciences*. Springer, Berlin, 2004.

[12] A. Garzón, R. O. Grigoriev, and F. H. Fenton. Model-based control of cardiac alternans in Purkinje fibers. *Physical Review E*, 84(4):041927, 2011.

[13] A. R. M. Gelzer, M. L. Koller, N. F. Otani, J. J. Fox, M. W. Enyeart, G. J. Hooker, M. L. Riccio, C. R. Bartoli, and R. F. Gilmour Jr. Dynamic mechanism for initiation of ventricular fibrillation in vivo. *Circulation*, 118(11):1123, 2008.

[14] W. Groenendaal, F. A. Ortega, T. Krogh-Madsen, and D. J. Christini. Voltage and calcium dynamics both underlie cellular alternans in cardiac myocytes. *Biophysical Journal*, 106(10):2222–2232, 2014.

[15] J. Guckenheimer. Isochrons and phaseless sets. *Journal of Mathematical Biology*, 1(3):259–273, 1975.

[16] J. Guckenheimer and P. Holmes. *Nonlinear Oscillations, Dynamical Systems, and Bifurcations of Vector Fields*, volume 42. Springer Verlag, New York, 1983.

[17] J. P. Hespanha. *Linear Systems Theory*. Princeton University Press, Princeton, New Jersey, 2018.

[18] A. B. Holt, D. Wilson, M. Shinn, J. Moehlis, and T. I. Netoff. Phasic burst stimulation: a closed-loop approach to tuning deep brain stimulation parameters for parkinson's disease. *PLoS Computational Biology*, 12(7):e1005011, 2016.

[19] E. M. Izhikevich. *Dynamical Systems in Neuroscience: The Geometry of Excitability and Bursting*. MIT Press, London, 2007.

[20] D. Jordan and P. Smith. *Nonlinear Ordinary Differential Equations: An Introduction for Scientists and Engineers*, volume 10. Oxford University Press, Oxford, 2007.

[21] D. Kirk. *Optimal Control Theory*. Dover Publications, New York, 1998.

[22] I. Z. Kiss, C. G. Rusin, H. Kori, and J. L. Hudson. Engineering complex dynamical structures: sequential patterns and desynchronization. *Science*, 316:1886–1889, 2007.

[23] T. Krogh-Madsen and D. J. Christini. Action potential duration dispersion and alternans in simulated heterogeneous cardiac tissue with a structural barrier. *Biophysical Journal*, 92(4):1138–1149, 2007.

[24] N. J. Kutz, S. L. Brunton, B. W. Brunton, and J. L. Proctor. *Dynamic Mode Decomposition: Data-Driven Modeling of Complex Systems*. Society for Industrial and Applied Mathematics, Philadelphia, PA, 2016.

[25] B. Lusch, N. J. Kutz, and S. L. Brunton. Deep learning for universal linear embeddings of nonlinear dynamics. *Nature Communications*, 9(1):1–10, 2018.

[26] A. Mauroy, I. Mezić, and J. Moehlis. Isostables, isochrons, and Koopman spectrum for the action–angle representation of stable fixed point dynamics. *Physica D: Nonlinear Phenomena*, 261:19–30, 2013.

[27] I. Mezić. Analysis of fluid flows via spectral properties of the Koopman operator. *Annual Review of Fluid Mechanics*, 45:357–378, 2013.

[28] I. Mezić. Spectrum of the Koopman operator, spectral expansions in functional spaces, and state-space geometry. *Journal of Nonlinear Science*, pages 1–55, 2019.

[29] B. Monga, D. Wilson, T. Matchen, and J. Moehlis. Phase reduction and phase-based optimal control for biological systems: a tutorial. *Biological Cybernetics*, 113(1-2):11–46, 2019.

[30] A. Nabi, T. Stigen, J. Moehlis, and T. Netoff. Minimum energy control for *in vitro* neurons. *Journal of Neural Engineering*, 10(3):036005, 2013.

[31] S. M. Narayan. T-wave alternans and the susceptibility to ventricular arrhythmias. *Journal of the American College of Cardiology*, 47(2):269–281, 2006.

[32] D. Noble. A modification of the Hodgkin-Huxley equations applicable to Purkinje fibre action and pacemaker potentials. *The Journal of Physiology*, 160(2):317–352, 1962.

[33] J. B. Nolasco and R. W. Dahlen. A graphic method for the study of alternation in cardiac action potentials. *Journal of Applied Physiology*, 25(2):191–196, 1968.

[34] E. J. Pruvot, R. P. Katra, D. S. Rosenbaum, and K. R. Laurita. Role of calcium cycling versus restitution in the mechanism of repolarization alternans. *Circulation Research*, 94(8):1083–1090, 2004.

[35] K. Pyragas. Continuous control of chaos by self-controlling feedback. *Physics Letters A*, 170(6):421–428, 1992.

[36] Z. Qu, A. Garfinkel, P. Chen, and J. N. Weiss. Mechanisms of discordant alternans and induction of reentry in simulated cardiac tissue. *Circulation*, 102(14):1664–1670, 2000.

[37] W.J. Rappel, F. Fenton, and A. Karma. Spatiotemporal control of wave instabilities in cardiac tissue. *Physical Review Letters*, 83(2):456, 1999.

[38] J. A. Sanders, F. Verhulst, and J. Murdock. *Averaging Methods in Nonlinear Dynamical Systems*. Springer-Verlag, New York, second edition, 2007.

[39] P. J. Schmid. Dynamic mode decomposition of numerical and experimental data. *Journal of Fluid Mechanics*, 656:5–28, 2010.

[40] E. Schöll and H. G. Schuster. *Handbook of Chaos Control*, volume 2. Wiley, 2008.

[41] K. Serkh and D. B. Forger. Optimal schedules of light exposure for rapidly correcting circadian misalignment. *PLoS Computational Biology*, 10(4):e1003523, 2014.

[42] K. Taira, S. L. Brunton, S. T. M. Dawson, C. W. Rowley, T. Colonius, B. J. McKeon, O. T. Schmidt, S. Gordeyev, V. Theofilis, and L. S. Ukeiley. Modal analysis of fluid flows: an overview. *AIAA Journal*, pages 4013–4041, 2017.

[43] E. J. Vigmond, F. Aguel, and N. A. Trayanova. Computational techniques for solving the bidomain equations in three dimensions. *IEEE Transactions on Biomedical Engineering*, 49(11):1260–1269, 2002.

[44] M. A. Watanabe, F. H. Fenton, S. J. Evans, H. M. Hastings, and A. Karma. Mechanisms for discordant alternans. *Journal of Cardiovascular Electrophysiology*, 12(2):196–206, 2001.

[45] J. N. Weiss, A. Karma, Y. Shiferaw, P. Chen, A. Garfinkel, and Z. Qu. From pulsus to pulseless: the saga of cardiac alternans. *Circulation Research*, 98(10):1244–1253, 2006.

[46] M. O. Williams, I. G. Kevrekidis, and C. W. Rowley. A data–driven approximation of the Koopman operator: Extending dynamic mode decomposition. *Journal of Nonlinear Science*, 25(6):1307–1346, 2015.

[47] D. Wilson. Isostable reduction of oscillators with piecewise smooth dynamics and complex Floquet multipliers. *Physical Review E*, 99(2):022210, 2019.

[48] D. Wilson. An optimal framework for nonfeedback stability control of chaos. *SIAM Journal on Applied Dynamical Systems*, 18(4):1982–1999, 2019.

[49] D. Wilson. A data-driven phase and isostable reduced modeling framework for oscillatory dynamical systems. *Chaos: An Interdisciplinary Journal of Nonlinear Science*, 30(1):013121, 2020.

[50] D. Wilson. Phase-amplitude reduction far beyond the weakly perturbed paradigm. *Physical Review E*, 101(2):022220, 2020.

[51] D. Wilson and B. Ermentrout. Greater accuracy and broadened applicability of phase reduction using isostable coordinates. *Journal of Mathematical Biology*, 76(1-2):37–66, 2018.

[52] D. Wilson and B. Ermentrout. An operational definition of phase characterizes the transient response of perturbed limit cycle oscillators. *SIAM Journal on Applied Dynamical Systems*, 17(4):2516–2543, 2018.

[53] D. Wilson and B. Ermentrout. Augmented phase reduction of (not so) weakly perturbed coupled oscillators. *SIAM Review*, 61(2):277–315, 2019.

[54] D. Wilson and B. Ermentrout. Phase models beyond weak coupling. *Physical Review Letters*, 123(16):164101, 2019.

[55] D. Wilson and J. Moehlis. Spatiotemporal control to eliminate cardiac alternans using isostable reduction. *Physica D: Nonlinear Phenomena*, 342:32–44, 2017.

[56] A. Winfree. *The Geometry of Biological Time*. Springer Verlag, New York, second edition, 2001.

[57] E. Yeung, S. Kundu, and N. Hodas. Learning deep neural network representations for Koopman operators of nonlinear dynamical systems. In *2019 American Control Conference*, pages 4832–4839. IEEE, 2019.